IEEE Access
Multidisciplinary | Rapid Review | Open Access Journal

Received 9 May 2024, accepted 27 May 2024, date of publication 4 June 2024, date of current version 12 June 2024.

Digital Object Identifier 10.1109/ACCESS.2024.3409424

RESEARCH ARTICLE

Performance Assessment of Underwater-to-Air Optical Wireless Communication System With the Effect of Solar Noise and Sea Surface Conditions

BHOGESWARA RAO ANGARA[1,2], PALANISAMY SHANMUGAM[1], HARISHANKAR RAMACHANDRAN[2], AND CHAVAPATI GOUSE SANDHANI[1]

[1]Department of Ocean Engineering, Indian Institute of Technology Madras, Chennai 600036, India
[2]Department of Electrical Engineering, Indian Institute of Technology Madras, Chennai 600036, India

Corresponding author: Palanisamy Shanmugam (pshanmugam@iitm.ac.in)

This work was supported by the Ministry of Human Resource Development (MHRD) Fellowship through the Interdisciplinary Research Program (IDRP) with the Indian Institute of Technology (IIT) Madras.

ABSTRACT This study focuses on the performance evaluation of underwater-to-air Optical Wireless Communication (OWC) and data transmission between Autonomous Underwater Vehicles (AUVs) and Autonomous Aerial Vehicles (AAVs). Facing challenges from the harsh marine environment and optical signal attenuation, we utilized Monte Carlo (MC) simulations to comprehensively assess the system performance. Our investigation incorporated crucial elements impacting signal attenuation, including particulate matter, bubbles, rough sea conditions, and solar noise. By integrating the in-situ Inherent Optical Properties (IOPs) data and Hall-Novarini (HN) model for bubble characteristics, we constructed a robust simulation framework. To accurately estimate optical beam fluctuations caused by surface waves, we employed the three-dimensional theoretical ECKV (Elfouhaily, Chapron, Katsaros, and Vandemark) model for the water-air interface layer. The received power calculated for varying wind conditions, with and without bubbles, revealed fluctuations attributed to surface waves' interaction with the optical signal. Moreover, we observed a decrease in received power due to the bubble effects and the water-air interface layer. Solar radiation's significant impact on the transmitted signal, especially at the airborne receivers, was evident through the BER performance analysis. We conducted extensive experiments for measuring the solar radiance and evaluating its influence on the BER performance, particularly noting degradation during zenith sun positions and increased errors in scenarios with higher solar glint. Additionally, our investigation highlighted the adverse effect of sea surface bubbles on received solar power and the findings revealed that the BER performance is significantly reduced in the presence of bubbles rather than the scenarios without bubbles.

INDEX TERMS Optical wireless communication, Monte Carlo, optical properties, bubbles, solar noise, oceanic water.

I. INTRODUCTION

Underwater-to-air Optical Wireless Communication (OWC) is a rapidly growing field because of its significant impacts across a range of industries. It enables real-time data transfer from the submerged source to the surface systems, supporting scientific research, environmental monitoring, national security, and industrial/maritime applications. Underwater Optical Wireless Communications (UOWC) offer high bandwidth, making it a foundational tool for diverse applications due to the weak absorption of the water in the blue-green wavelength region [1], [2]. Traditional methods

The associate editor coordinating the review of this manuscript and approving it for publication was Yougan Chen.

© 2024 The Authors. This work is licensed under a Creative Commons Attribution-NonCommercial-NoDerivatives 4.0 License.
For more information, see https://creativecommons.org/licenses/by-nc-nd/4.0/

like acoustic [3], [4] and radio waves [5], [6] have limitations in data rate and propagation. There is a growing interest in exploring and exploiting marine natural resources, which require an improved UOWC system for communication within/between the underwater sensor networks, autonomous underwater vehicles (AUVs), remotely-operated vehicles (ROVs), and from submarines to autonomous aerial vehicles (AAVs). UOWC is a promising technology for such applications, offering high data rates, low latency, and energy-efficient communication links [7], particularly in clear waters with distances of up to approximately 150 m [8], [9].

Earlier researchers have conducted comprehensive studies on modelling the downlink (air-to-underwater) and underwater-to-underwater OWC channel in various ocean waters. When modelling the downlink UOWC channel, researchers employed the Cox and Munk method to model the sea surface. Nevertheless, this method lacks essential spatial and temporal correlated information necessary for accurately modelling the channel for laser communication. Furthermore, their investigations were carried out without considering solar noise. However, as of now, there have been no studies conducted on modeling the underwater-to-air OWC channel. The study of underwater-to-air OWC systems is of paramount importance due to the increasing demand for real-time applications in underwater environments. In scenarios such as underwater sensor networks and AUVs, the need for timely and efficient transmission of data from the underwater devices to the surface is crucial. This underwater-to-air communication plays a vital role in applications where instant data collection and monitoring are required, driving the focus on enhancing the reliability and efficiency of the uplink UOWC systems to meet the growing demands of real-time underwater communication.

In underwater-to-air OWC systems, there is a significant challenge posed by an optical pathway transition from the underwater environment to the above-surface air medium. The wavy ocean surface produced by wind fields represents one of the major constraints that impact the reliability and performance of communication links. Wind-induced waves, currents, and other environmental factors create disturbances in the water-air interface layer, which can lead to fluctuations in the refractive index gradient at the water-air interface and cause scattering, diffraction, and turbulence in the optical signal. Researchers have developed various models to describe the air-sea interface and its impact on optical communication. These models aim to simulate and understand the behaviour of light as it traverses through this complex boundary. Some of the commonly used sea surface models include the Boussinesq and Korteweg-de Vries (KdV) model [10], Cox and Munk model [11] and Fast Fourier Transform (FFT) approximation [12]. The air-sea interface models find extensive applications, particularly in remote sensing. They play a crucial role in estimating various parameters, including bidirectional transmission and reflectance distribution functions (BTDF and BRDF) [13], [14]. These models have proven useful in understanding how the reflected light from the sea surface impacts our observations, especially when conditions such as sky radiance and sun glint are present. Further, these models have been used to analyse the water-leaving radiance in different atmospheric and marine conditions [15], [16]. Earlier studies have relayed on the probabilistic sea surface models, originally developed by Cox and Munk, to study the effect of the air-sea interface [14], [17], [18]. Numerous studies have utilised the Cox and Munk model to analyse UOWC vertical links, particularly when the light beam propagates from the air medium (atmosphere) to the underwater environment. These studies observed that the greater variability in sea surface slopes due to wind speed (u) reduces the system performance, which resulted in higher power loss and increased bit error rates [19], [20], [21]. Studies have also utilised the KdV equations to simulate the air-sea interface with an aim to analyse the coverage area of an optical beam as it propagates from the air into the underwater environment, considering the presence of multiple light sources located in the air medium [22]. In a controlled laboratory setting, experiments were conducted to study a short-range (0.66 m) water-to-air OWC link. These experiments indicated fluctuations in the channel link gain under both calm and wavy surface conditions [23]. In recent studies [24], researchers have developed a model to simulate the vertical UOWC channel. This model takes into account several factors simultaneously: oceanic turbulence parameters, real-time depth-dependent temperature and salinity, chlorophyll concentration, and the presence of bubbles. Additionally, it considers the transmitter beam's oblique incidence at various angles. The findings indicate that the scintillation index rises as the transmitter tilt angle increases. The study [25] evaluates UOWC links with on-off key modulation and selection combining (SC) receive diversity under underwater conditions. It derives closed-form expressions for BER and outage probability, validated through simulations, showing SC diversity mitigates beam attenuation effects. The study [26] examines vertical UOWC links affected by non-mixing layers due to ocean stratification, causing turbulence variations. It models the channel as a concatenation of these layers, deriving closed-form expressions for BER and analysing diversity gains. Results reveal inaccuracies in assuming constant turbulence strength and provide insights into the effect of layering on capacity. Another study [27] explores the performance of vertical UWOC systems amidst air bubbles and temperature gradients. A layered structure with N layers is employed to model the vertical channel's turbulence inhomogeneity using an exponential generalised gamma distribution. Asymptotic average BER and ergodic capacity are derived using H-functions and validated through simulation results. In our most recent investigation [28], we thoroughly examined how sea surface waves and bubbles affect underwater-to-air OWC systems. Our analysis

indicates a substantial variation in received power, depending on the wind speed above the sea surface.

Another challenge in modelling the underwater-to-air OWC channel is the presence of oceanic bubbles. These bubbles are generated by breaking waves in the upper ocean [29], [30] and penetrate the lower water column at depths over several meters, strongly contingent on wind speeds [31]. As a consequence of these bubbles in the upper ocean layer, the light beam is randomly affected and attenuated when passing through the bubble layer. Under high wind speeds, bubble scattering is rapidly enhanced and even more pronounced than particulate scattering in the air-water interface layer. Thus, it is crucial to understand the effect of bubbles on the performance of the underwater-to-air OWC system. Numerous studies revealed a substantial degradation in UOWC system performance in the presence of bubbles (including clean-coated variants) of varying sizes under different wind speeds [19], [32].

Another significant effect on the UOWC system is the interference of solar radiation with an optical signal received by a photodetector. This interference is particularly more pronounced when the receiver is situated in the atmosphere/air medium rather than in the underwater environment. The spectrum of sunlight covers the entire visible wavelength range and beyond in clear marine environments with high water transparency, and it can penetrate several meters of water. Particularly, longer blue to shorter green wavelengths of light can penetrate deeper into the water due to low absorption of water, which allows the penetrating radiation to be easily detectable by sensitive detectors even at depths exceeding 600 m [33]. Previous studies have not paid much attention to the influence of solar noise on the UOWC performance. However, recent work has highlighted background noise's impact and how it affects the UOWC system through various factors like the link length, receiver field of view, and different types of photodetectors [34], [35], [36], [37], [38]. In [34], the significant impact of solar light interference on the UOWC system performance was focused, and effective noise cancellation techniques were emphasised to optimise the UOWC systems in high-intensity solar light conditions. This domain becomes more complex when the receiver is located in the air medium, where it is exposed to solar noise influenced by several factors, including sky radiance, sea surface roughness, water-leaving radiance (depending on the wind speed and wave shape), the time of day, and sun glint.

In this study, our main focus is to incorporate the above factors into the channel model and investigate the performance of underwater-to-air OWC system under different ocean and surface conditions. The Monte-Carlo (MC) technique is employed to simulate the underwater-to-air OWC system with in-situ optical data collected from oceanic waters in the Bay of Bengal and Southern Ocean. Ocean bubble characteristics are determined using the widely recognised Hall-Novarini (HN) model [39], and the distribution of bubble sizes and their ability to penetrate deeper into water depends upon the prevailing wind speed. Recognising the limitations of the Cox and Munk sea surface model, which lacks spatial and temporal correlation information, we utilise the ECKV sea surface model because of its ability to incorporate both spatial and temporal correlation data. This information is essential in understanding how the light beam propagates through the air-sea interface. We assess the solar interference experienced by the receiver by analysing the radiometric data collected above and below the water surface. These data were collected at various times of the day and under different sea conditions, including calm waters, wavy surfaces, and conditions with wind-induced bubbles. Our analysis reveals that the amount of solar power captured by the receiver varies significantly depending on these parameters.

In addition, we examine the correlation between received power, wind speed, and wind-induced bubbles in an underwater-to-air OWC system. The results are compared across a range of sea surface conditions. Finally, the BER performance of underwater-to-air OWC systems was assessed, considering the individual and combined effects of waves, wind-induced bubbles, and varying levels of solar interference.

II. UNDERWATER-TO-AIR OWC SYSTEM MODEL

This section presents the concepts of an underwater-to-air OWC system under investigation (Fig. 1) and describes the key components of the models considered in this study. Here, the transmitter (laser source) is positioned at a specific distance beneath the sea surface, while the receiver is situated several meters above the sea surface. As the optical signal propagated from the source to the destination, it can undergo attenuation due to the various phenomena depicted in Fig. 1. Thus, it becomes crucial to comprehend the underlying theories related to sea surface models, solar noise models, the mechanisms involving bubbles in seawater, and the inherent optical properties (IOPs) of seawater. The fundamental IOPs include absorption (a), scattering (b), and attenuation ($c = a + b$) coefficients and scattering phase function, which collectively play a pivotal role in characterising the optical behaviour of seawater. These parameters were employed as the essential inputs in our MC method for effectively simulating the propagation of photons within the water column.

A. SEA SURFACE GENERATION USING ECKV MODEL

The two-dimensional ECKV (Elfouhaily, Chapron, Katsaros, and Vandemark) spectrum serves as a fundamental tool in oceanography and sea surface modelling [12]. It provides a spectral description of wave energy distribution, which is used to generate realistic sea surfaces through a combination of mathematical operations and random phase introduction. Its applications extend beyond sea surface generation to include areas like remote sensing, environmental impact assessment, and the study of nonlinear wave effects. To obtain the sea surface elevation $z\left(x_i, y_j\right)$, the points on the sea surface grid are sampled in a region of size L_x by L_y m with N_x and N_y points along x and y-directions, respectively,

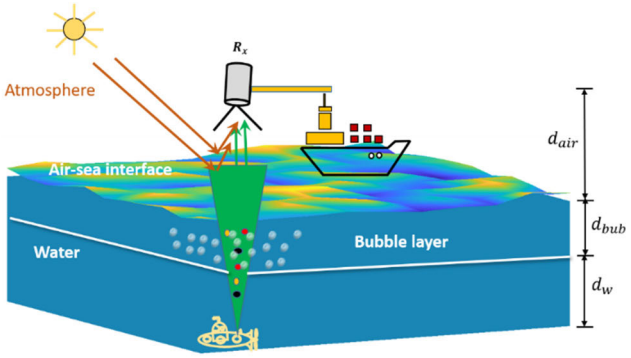

FIGURE 1. Schematic of the channel model for the underwater-to-air OWC system.

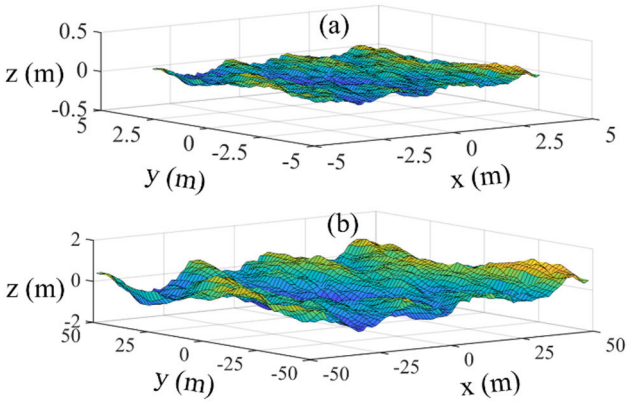

FIGURE 2. The sea surface realisations using the ECKV model for a wind speed of a) 3 m s^{-1} b) 10 m s^{-1}.

as given by

$$z\left(x_i, y_j\right) = \sum_{u=o}^{N_x-1} \sum_{v=0}^{N_y-1} \hat{z}(u, v) e^{i2\pi(x_i u/N_x + y_j v/N_y)} \quad (1)$$

where the harmonic components $\hat{z}(u, v)$ are indexed by u and v in the wavenumber k domain. For an understanding of the ECKV sea surface model, the theoretical foundations and derivations of this model can be found in a previous study [12].

The process of generating a sea surface using the ECKV spectrum involves several key steps. First, it requires the computation of the two-sided discrete values of the elevation variance, which essentially quantifies how wave energy is distributed across different frequencies and directions in the ocean. Next, in order to create a realistic sea surface, the simulation employs random sampling techniques. Specifically, it samples the amplitudes of the harmonic components from normal distributions. This introduces variability and randomness into the wave field while preserving the spectral characteristics defined by the ECKV spectrum. Finally, to translate the spectral information into the spatial domain and obtain the sea-surface elevation in two dimensions, the Inverse Fast Fourier Transform (IFFT) is employed. This mathematical operation is essential for generating a detailed representation of the sea surface, complete wave crests, troughs, and their variations across space and time. These three interconnected steps collectively contribute to the creation of a realistic and dynamic sea surface based on the ECKV spectrum.

The ECKV model originates from the linear superposition theory and excels in accurately representing the complex dynamics of the ocean's surface. The ECKV model integrates both spatial (between adjacent triangle vertices) and temporal (from one time step to the next) correlation information into the generated sea surface model. Thus, it is crucial to understand the spatial and temporal correlation of sea surface data in order to gain insights into the propagation of laser beams across the water-air interface. The sea surfaces generated using the ECKV method, with wind speeds of 3 and 10 m s^{-1}, are depicted in Fig. 2. As the wind speed increases, the sea surface becomes progressively rougher. Consequently, the mean square slope value, which quantifies the degree of surface roughness, increases in direct correlation with higher wind speeds.

B. PHOTON PROPAGATION THROUGH THE WATER, WATER-AIR INTERFACE AND AIR USING MONTE-CARLO METHOD

The MC approach is invaluable for modelling and understanding the complex interactions between light and water, finding diverse applications that extend to areas like underwater communication. Figure 3 illustrates the key steps of Monte Carlo simulations used to model the propagation of photons from underwater to air medium. In the MC simulation method for photon propagation in a water column, several key steps are involved. First, the optical properties of water, including the absorption (a), scattering (b) and attenuation (c) coefficients, are defined. Next, the photon's initial position and direction are determined. The simulation then progresses through discrete steps, with the photon's trajectory being probabilistically determined based on these properties. At each step, the photon's interactions with the medium are governed by the scattering or absorption events, contingent upon the scattering albedo ($\omega = b/c$) condition. The probabilities for these interactions are calculated using the relevant optical properties. When the photon moves within the water column, whether it is absorbed or scattered is determined by comparing a randomly generated number ξ, drawn from a uniform distribution [0 1], with the albedo value (ω). If ξ is less than or equal to ω, the photon undergoes scattering; otherwise, it is absorbed by the water particles. In instances where a photon is scattered by a water particle or bubble, the scattering angle is determined by referencing the respective volume scattering function (VSF). A detailed discussion about the MC rules for photon propagation through the water medium and air-sea interface is given in [19] and [21]. In these simulations, we generated sea surface models using the ECKV method, which relies on the FFT technique. The sea surface is generated with an optimal selection of

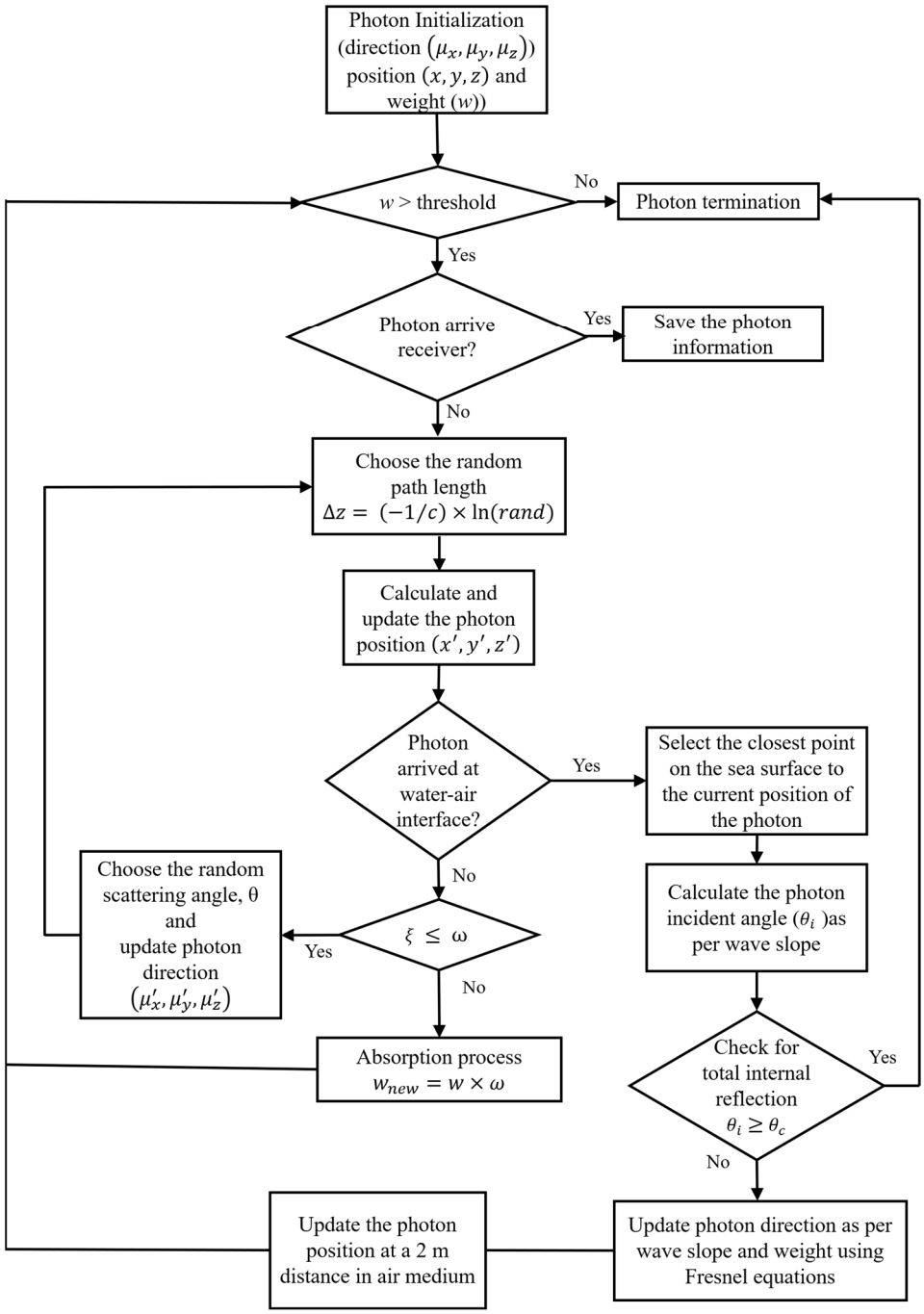

FIGURE 3. A flowchart of photon propagation from the underwater-to-air OWC system.

spatial grid resolution, a choice that depends on both wind speed and maximum wavelength of the wave.

During the photon's propagation, once it has traversed a distance of (d_w+ d_{bub}) m within the water and bubble layer and reached the sea surface, the simulation identifies the point on the sea surface that is closest to the photon's current position. The photon's position is then updated accordingly, with the simulation choosing the point on the sea surface that offers the minimum distance from the photon's current location. To compute the normal vectors ($\hat{n}$) of the sea surface at individual grid points, we employ bicubic interpolation. This involves first applying a bicubic data fitting process to grid data. Subsequently, we derive diagonal vectors and employ them to ascertain the surface normal at each vertex through a cross-product operation. We determine the angle at which a photon strikes the wave surface, denoted as (θ_i), by taking the scalar product of two vectors: the unit normal vector ($\hat{n}$) and the direction cosine vector ($\hat{\mu}_i$) representing

the photon's direction just before it reaches the water-air interface.

Subsequently, we calculate the angle of transmittance (θ_t) and the transmission coefficient (ρ) specific to the wave facet. These values are derived using the Snell's law and Fresnel equations [21], which provides essential insights into the photon's behaviour as it interacts with the wave.

As the photon travels a distance of a few meters through the air before reaching the receiver, our working assumption is that the maritime clear atmosphere remains free from particulate matter. This implies that during its propagation, the photon encounters no significant attenuation ($c \approx 0.9 \times 10^{-4}\text{m}^{-1}$) phenomena that would alter its path or intensity.

C. IN-SITU IOPS OF SEAWATER WITH AND WITHOUT BUBBLES

Previous studies have relied on the constant (single) values of absorption and scattering coefficients, typically derived from the Petzold measurements. However, these values are suitable for horizontal UOWC links. For vertical links, it is important to note that the attenuation and scattering profiles are not constant as these coefficients vary with depth due to the particulate matters (including sediments, phytoplankton, detritus, and bubbles concentrated in the upper sea surface layers). These IOPs were determined through the measurements obtained from optical instruments (such as the Wet Lab's ACS and LISST-VSF) in Bay of Bengal waters. These measurements were used as the inputs for MC simulations. The in-situ measurements were collected under normal sea state conditions without much bubbles. Statistical information regarding the bubbles was obtained from the HN model [39]. The IOPs of oceanic bubbles were then calculated using the HN model and methods established in earlier studies [31].

The VSF data, which include the influence of bubbles (following a power law distribution), were also taken from the measurements conducted in Southern Ocean waters [40]. These measurements were collected in clear waters where the concentrations of chlorophyll and total suspended matter were recorded as 0.72 mg m^{-3} and 0.5 g m^{-3} respectively. The scattering phase function data were obtained by normalising the VSF values with the scattering coefficients. The resulting scattering phase functions are shown in Fig. 4, where bubbles exhibit distinct scattering characteristics. The results indicate a higher probability of scattering at larger angles in the presence of bubbles compared to the cases without bubbles.

Figure 5 presents the depth profiles of both total scattering (b_t) and attenuation coefficients (c_t), which were measured in open sea waters of the Bay of Bengal. For this study, we considered a bubble distribution that reflects the prevalent bubble sizes under real-time oceanic conditions. These bubbles follow a power law distribution characterised by the minimum (r_{min}) and maximum bubble sizes (r_{max}) of 5 μm and 200 μm respectively, with a distribution slope (α) of - 4.

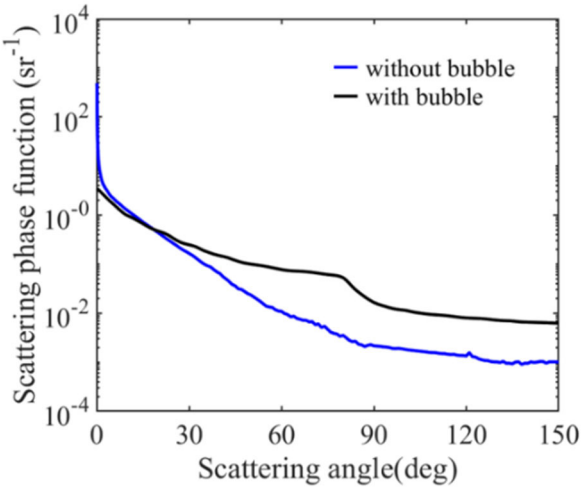

FIGURE 4. Scattering phase functions compared between bubble-free Bay of Bengal waters and bubble-containing Southern Ocean waters.

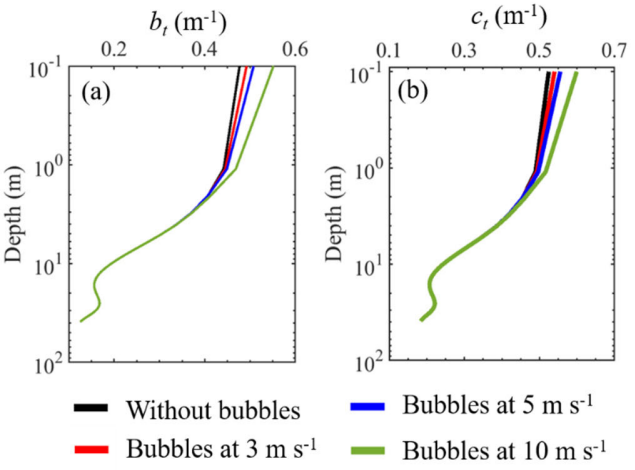

FIGURE 5. Depth profiles of (a) scattering and (b) attenuation coefficients collected in Bay of Bengal waters (with and without bubbles).

Assuming the absorption coefficient of bubbles being negligible, the scattering coefficients of bubbles were calculated using [41]

$$b_{bub}(z) = N(z)\,\bar{Q}_{sca}\bar{S} \tag{2}$$

where N(z) represents the bubble density at a given depth (z) within the water column, which was calculated using the HN model, $\bar{S}$ denotes the geometric mean cross-sectional area of bubbles and $\bar{Q}_{sca}$ represents the mean scattering efficiency.

The measurements indicate that both b_t and c_t values decrease towards the deeper water column as a result of decreasing particulate matter concentrations. Additionally, with an increase in wind speed, there is an increase in the number density of bubbles $N(z)$. Consequently, this leads to an increase in the scattering and attenuation coefficients attributed to bubbles (according to Eq. 2).

D. SOLAR NOISE MODELLING

To quantify the solar radiance received by the receiver (positioned a few meters above the sea surface and looking vertically downward toward the air/water boundary), we evaluated its influence on the performance of the underwater-to-air OWC system by analysing the total upwelling solar radiance spectrum (denoted as $L_t(\theta, \lambda)$ in units of W m^{-2} nm^{-1} sr^{-1}, where λ and θ represent the wavelength and solar zenith angle respectively). Due to the position of receiver in the air medium, the optical signal of reflected solar radiation (direct and diffuse reflection and the sky) and transmitted through the water-air interface is collected by the receiver. Figure 6 shows the various processes contributing to the total upwelling solar radiance (L_t), which includes the surface reflected sky radiance (L_s), surface reflected radiance (L_g) due to sun glint, and water-leaving radiance (L_w). The surface-reflected solar radiance is the direct reflection of sun glint and sky radiation from the water surface. The water-leaving radiance (L_w) is the upwelling radiance emerging from the water column, which is a fraction of solar radiation that penetrates the water. The total upwelling solar radiance is written as

$$L_t = L_w + L_s + L_g \tag{3}$$

1) DATA AND METHODS (RADIOMETRIC MEASUREMENTS)

The RAMSES TriOS hyperspectral radiometers were employed for collecting radiometric data from the above-surface and underwater setups. The above-surface dataset (Fig. 6 (b)) includes the measurements of sky radiance (L_{sky}), downwelling irradiance ($E_d(0^+)$), and total upwelling radiance (L_t) and the below-surface measurements (Fig. 6 (c)) include the downwelling irradiance $E_d(0^-)$ and upwelling radiance $L_u(0^-)$. The in-situ measurements of these properties were collected from Bay of Bengal waters during the daytime from 12 pm to 4 pm (local time, IST). While the direct measurements of L_t are available within the dataset, these data do not provide sufficient insights into the influence of specific parameters like L_w, L_s and L_g on the solar power captured by the receiver. As illustrated in Fig. 6 (a), these radiance (L_w, L_s and L_g) values are influenced by numerous marine environmental factors (including sea surface roughness, wind speed, sun glint intensity, and bubble size/concentrations near the sea surface). Thus, it becomes essential to thoroughly investigate the effects of these parameters on the modelling of the underwater-to-air OWC system's performance. Our in-situ measurements strictly followed the ocean optics protocols and methods presented in Mobley [42], where the radiance sensor was fixed at an angle of 40° from nadir and approximately 135^0 azimuth from the sun (see Fig. 6 (b)). The surface-reflected radiance (L_s) can be calculated based on the L_{sky} values using

$$L_s = \rho L_{sky} \tag{4}$$

Here, ρ represents the Fresnel reflectance coefficient at the air-sea interface, indicating the proportion of light reflected

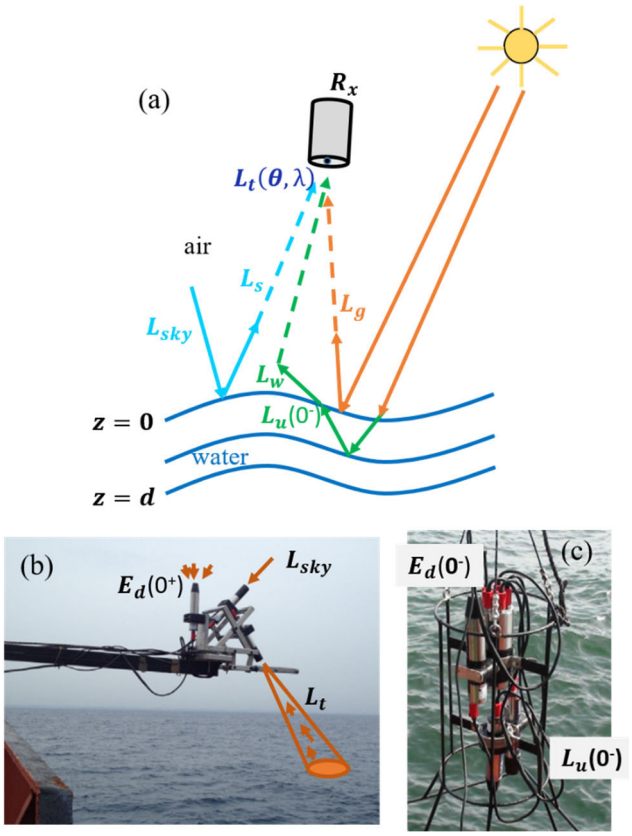

FIGURE 6. (a) Illustration of various processes contributing to the total upwelling solar radiance, (b) Field setup of RAMSES-Trios above-surface radiometers (downwelling irradiance E_d (0^+), sky radiance L_{sky}, and total upwelling radiance L_t) on an extended platform for measurements, (c) Field setup of RAMSES-Trios underwater radiometers installed on an underwater frame for measuring downwelling irradiance E_d (0^-) and upwelling radiance L_u (0^-) below the sea surface.

from the sea surface. Its value typically varies with the factors such as wavelength, wave shape, wind speed, solar zenith angles, and specific viewing geometry [42], [43]. In the case of a flat sea surface and a uniform sky radiance distribution, the value of ρ is 0.02 for a sensor viewing angle (θ) less than 30^0 and increases to 0.03 when θ equals 40^0 [44]. However, the sea surface is often wave-roughened through the combined influence of wind's energy transfer to waves, the inherent turbulence within these waves, and the length of the wind's path over the water. Consequently, this variability underscores that the parameter ρ cannot remain constant and is often greater than the values mentioned earlier. Thus, ρ cannot be a constant value and it is larger than the reported values. Additionally, it is clear that determining this parameter across diverse wind and sea conditions presents a significant scientific challenge. Because of this complex nature, many researchers have considered a fixed value of $\rho = 0.028$ as previously suggested by Mobley [42]. This is typically done under the conditions of a uniform sky radiance distribution, low wind speeds (less than 5 m s^{-1}), viewing angles not exceeding 40^0, and with no influence from sunlight reflection off the sea surface (sun glint). In this study,

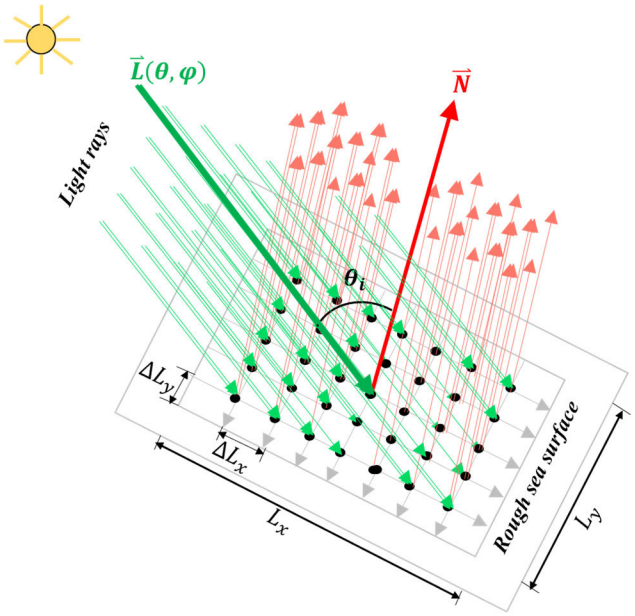

FIGURE 7. Schematic diagram of calculating ρ from the sea surface model.

we determined the ρ value by employing the ECKV method to model the sea surface. We conducted these calculations for a range of solar zenith angles and wind speeds. This approach was necessary because the sea surface roughness varies with changing wind speed and direction, and the intensity of incident sunlight on the sea surface varies with changing solar zenith angles and time intervals. Solar zenith angles can be determined by considering both the time of day and the geographical location and hence vary accordingly. The schematic diagram of calculating the ρ values from the sea surface model is shown in Fig. 7. When parallel sunlight strikes the mesh grid of the sea surface, we calculate the incident angle ($\boldsymbol{\theta_i}$) between the incoming sun rays and the normal vector associated with the mesh grid point on the sea surface. The solar zenith angle (θ) is determined from the time of day, and the azimuthal angle (φ) is randomly generated within the interval of $[0, 2\pi]$. The ρ value is subsequently determined using Fresnel's equations, based on this angle of incidence.

In our study, we considered wind speeds at 3, 5, and 10 m s^{-1}. To accommodate the wavelength scales of capillary and gravity waves, we considered maximum wavelengths (L_x and L_y) of 8, 25, and 100 m for wind speeds of 3, 5 and 10 m s^{-1} respectively, based on a previous study [45]. To maintain the optimal grid resolution (ΔL_x and ΔL_y) of 0.09 cm, we sampled the sea surface at rates of 8192 × 8192, 32768× 32768, and 131072 × 131072 grid points for wind speeds of 3, 5, and 10 m s^{-1} respectively, depending on the values of L_x and L_y. To enhance the accuracy of determining the ρ values, we utilised 1000 different sea surface realisations modelled using the ECKV method for each wind speed in our simulations. Table 1 presents the average reflectance (ρ) value for various solar zenith angles and wind speeds. The calculations revealed that the ρ value is not constant, as previously assumed in earlier studies, but it varies with both the position of the sun and wind speeds. As the wind speed increases, the roughness of the sea surface also increases, causing the incident angles to diverge further and consequently leading to an increase in the average reflectance value. Further, it was observed that the ρ value increases as the solar zenith angle increases.

TABLE 1. The average reflectance (ρ) values for various solar zenith angles and wind speeds.

Solar zenith angles (θ_s)	Wind speed		
	3 m s^{-1}	5 m s^{-1}	10 m s^{-1}
25^0	0.035	0.052	0.104
30^0	0.043	0.063	0.111
45^0	0.081	0.100	0.129
60^0	0.139	0.146	0.149

As shown in Fig. 6 (a), the water-leaving radiances (L_w) were calculated using the underwater radiometer measurements by incorporating sea surface roughness on the upwelling radiance $L_u\left(0^-\right)$ just below the sea surface by using the following expression

$$L_w = \tau L_u\left(0^-\right) \tag{5}$$

where τ is the transmittance coefficient relative to the wave facet and is calculated using Snell's and Fresnel equations. As previously discussed, when calculating the value of τ, we applied the same principles as those used for calculating the ρ values. This implies that τ varies in response to changes in sea surface roughness and wind speed.

2) IMPACT OF BUBBLES ON THE RADIOMETRIC MEASUREMENTS

Wave breaking is a common phenomenon in open ocean waters, predominantly driven by winds. It results in the formation of bubbles on the sea surface, and the depth to which these bubbles penetrate the water column is influenced by both the characteristics of wind-generated waves and the concentrations of water constituents. To examine the impact of bubbles on the radiometric measurements, radiometric measurements were conducted continuously for approximately 3 minutes at a specific location in Bay of Bengal waters. For analytical purposes, the average data from these 3-minute measurements were utilised. These experiments were conducted on a bright sunny day, specifically from 12:00 pm to 4:00 pm (local time, IST), under two different water state conditions: calm water and wave-breaking-induced bubbles, as depicted in Fig. 8 (a) and (b). These measurements were collected at four different times: 12:20 pm, 1:25 pm, 2:45 pm, and 3:50 pm.

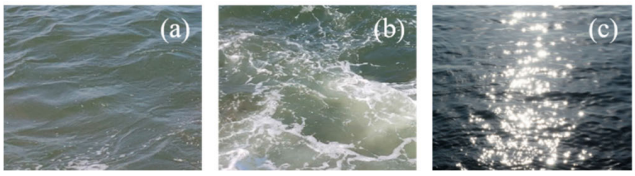

FIGURE 8. Images from field experiments in Bay of Bengal waters on February 15, 2020, between 12 pm and 3 pm, illustrating calm water and bubble cloud formation resulting from wave breaking. (a) calm water; (b) wave-induced bubble clouds; and (c) glint effect.

Figure 9 (a)-(c) displays the spectral sky radiance, downwelling irradiance, and upwelling radiance just below the sea surface at various time intervals in Bay of Bengal waters (all measurements made under clear sky conditions). Using the recorded time data and geographic location, we calculated the respective solar zenith angles (θ_s). These measurements clearly indicate a decreasing trend in spectral radiance and irradiance values as the daytime progresses. This decline in radiance and irradiance values is a direct result of the diminishing intensity of solar light, which decreases notably from 12:20 pm to 4 pm as the sun's position changes throughout the day. In Fig. 9 (c), the solid line corresponds to the upwelling spectral radiance observed under calm water conditions, while the dashed line represents the upwelling radiance spectrum when wave-breaking-induced bubbles formed. These distinct lines provide a clear contrast between the two scenarios, allowing for a comprehensive comparison of radiance spectra between calm and bubble-filled water states. The wave-breaking-induced bubbles typically result in higher radiance values compared to a calm water state because the bubbles scatter and reflect sunlight more effectively. The increased scattering and reflection contribute to higher radiance values.

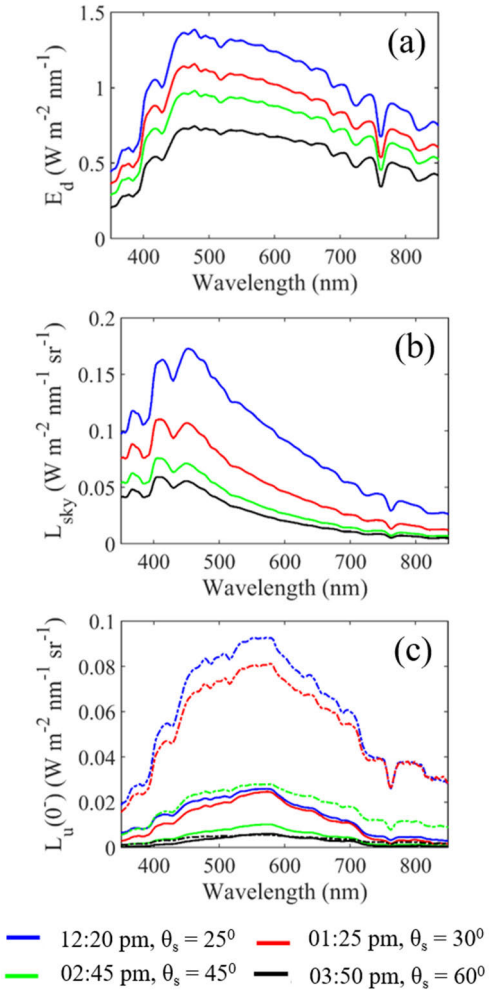

FIGURE 9. In-situ measurements collected at four different daytimes under clear sky conditions: (a) downwelling irradiance (E_d (0^+)), (b) sky radiance (L_{sky}), and (c) upwelling radiance (L_u (0^-)) just below the sea surface. Solid line - calm water radiance, dashed line - wave-breaking-induced bubbles radiance.

3) IMPACT OF SUN GLINT ON RADIOMETRIC MEASUREMENTS

Sun glint refers to the bright, reflective appearance of the sea surface when sunlight is directly reflected off it and towards an observer (such as a satellite or aircraft). This effect occurs due to the specular reflection of sunlight, where light is reflected at the exact angle it strikes the sea surface (as illustrated in Fig. 8 (c)). Even though the radiometric measurements are obtained taking the aforementioned precautions, it is still possible to detect sunlight reflected (sun glint) by the sea surface in the L_t data. Consequently, the surface reflected solar radiance encompasses not just the reflected sky light but also the sunlight reflected (sun glint) from the sea surface. In [44], the sun glint is calculated from the downwelling irradiance using

$$L_g = mE_d\left(0^+\right) \tag{6}$$

The parameter 'm' is a proportionality factor that signifies the magnitude of $E_d\left(0^+\right)$ in the in-situ radiometric data. It ranges between 0 and 0.07, with 'm' equalling 0 indicating the absence of glint conditions, while the higher values of 'm' correspond to the increased sun glint strength. Thus, the total upwelling radiance L_t reaching the sensor is expressed as

$$L_t = \tau L_u\left(0^-\right) + \rho L_{sky} + mE_d\left(0^+\right) \tag{7}$$

Figure 10 shows the variation in L_t as influenced by sun glint across a range of m values.

E. CALCULATING THE SYSTEM'S SIGNAL-TO-NOISE RATIO (SNR) AND BER PERFORMANCE USING AVALANCHE PHOTO DIODE (APD) RECEIVER

In our simulations, we utilised an Avalanche Photo Diode (APD) as a receiver to evaluate the BER performance of an underwater-to-air OWC system. The various electrical noises produced at the UOWC receiver are due to the thermal, shot and dark current noises. In [34], a complete model is presented for analysing the received noise in UOWC system. We used this model to calculate the received electrical noises for the case of APD detector. The APD receiver used

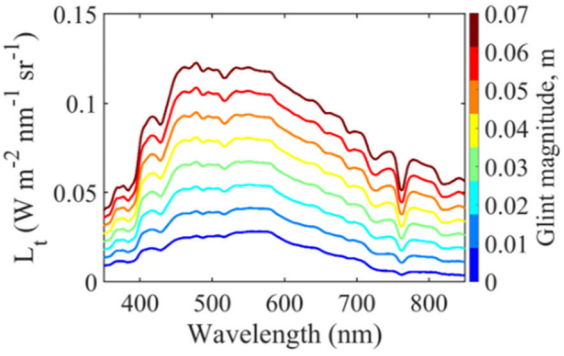

FIGURE 10. Variation in L_t as influenced by sun glint across various values of m.

the approximated zero mean Gaussian model and Poisson model for thermal and shot noises respectively. We reasonably assumed the dark current (I_d) values for APD as 10 nA. The thermal noise variance is given as

$$\sigma^2_{thermal} = \frac{4k_B T_m B_n}{R_{TIA}} \tag{8}$$

where B_n is the APD 's electrical bandwidth expressed in Hz, T_m is the medium temperature, R_{TIA} is the resistance of the trans-impedance amplifier's feedback resistor and k_B is Boltzmann constant.

Solar power reception is determined through the mathematical calculations using solar radiance spectra. This quantity, however, varies significantly based on several crucial parameters, including geographical location, time of day, the elevation or depth of the receiving equipment, and the aperture area's dimensions that are utilised for solar energy collection. The expression for the received solar power ($P_{R-solar}$) at the receiver is given as follows:

$$P_{R-solar} = L_t.T_\theta.A_{Apd}.\Delta\lambda.S \tag{9}$$

where T_θ represents the transmission efficiency of the filter, A_{Apd} is the effective area (m^2) of the receiver, $\Delta\lambda$ denotes the optical filter band width (nm), and S is the solid angle of the optical filter, measured in steradians. The expression for S in terms of the field of view (FOV) of the photo detector can be calculated using Eq. 10 and is given as follows:

$$S = 2\pi\left(1 - \cos\left(\frac{FOV}{2}\right)\right) \tag{10}$$

The variance of shot noise at the receiver due to the reception of both solar ($P_{R-solar}$) and signal power ($P_{R-signal}$) can be expressed as

$$\sigma^2_{shot} = 2qM^2_{APD}\begin{bmatrix} R_{APD}\left(P_{R-signal} + P_{R-solar}\right) \\ +I_d \end{bmatrix} B_n \tag{11}$$

where q is the electron charge, M_{APD} is the APD gain, R_{APD} is the responsivity of APD.

In addition to these two noises, two electrical beat noises ($\sigma^2_{sig-sol}, \sigma^2_{sol-sol}$) are generated at the detector using

$$\sigma^2_{sig-sol} = 4M_{APD}R^2_{APD}P_{R-signal}P_{R-solar}\frac{B_n}{BW_{opt}} \tag{12}$$

$$\sigma^2_{sol-sol} = R_{APD}\left(P_{R-signal}\right)^2\left[2 - \frac{B_n}{BW_{opt}}\right]\frac{B_n}{BW_{opt}} \tag{13}$$

where BW_{opt} is the bandwidth of the optical filter expressed in Hz.

The total variance of noise that occurs during the transmission of optical signal (bit '1') and no optical signal (bit '0') is expressed as

$$\sigma^2_{total,1} = \sigma^2_{shot} + \sigma^2_{thermal} + \sigma^2_{sig-sol} \tag{14}$$

$$\sigma^2_{total,0} = \sigma^2_{thermal} + 2qM^2_{APD}\left[R_{APD}\left(P_{R-solar}\right) + I_d\right]B_n \tag{15}$$

The SNR of the underwater-to-air OWC system is

$$SNR = \frac{\left[M_{APD}R_{APD}P_{R-signal}\left(1 - r_e\right)\right]^2}{\sigma^2_{total,1} + \sigma^2_{total,0}} \tag{16}$$

where r_e is the extinction ratio between optical power associated with bit '0' and '1', and the value is assumed as 0.1.

The performance of the underwater-to-air OWC system using OOK modulation can be expressed as [46]

$$BER = \frac{1}{2}erfc\left(\frac{\sqrt{SNR}}{2\sqrt{2}}\right) \tag{17}$$

where $erfc$ is the complementary error function.

III. RESULTS AND DISCUSSION

To quantify the effect of solar noise on the performance of the underwater-to-air OWC system, numerical results are presented for a range of scenarios, diverse oceanic conditions, varying receiver configurations, and atmospheric conditions. The parametric values for the transmitter and receiver used in our simulations are specified in Table 2. The selection of a green wavelength, specifically 515 nm, offers advantages for an UOWC system due to reduced absorption and enhanced signal transmission at this wavelength. This study employed the MC method using in-situ optical measurement data as the input parameters. Additionally, the HN model was integrated to account for bubble populations during the wave breaking events. In our simulations, the transmitter was situated 50 m below the sea surface and the receiver positioned 2 m above the sea surface. It was assumed that the transmitter is aligned with the receiver. In order to achieve a realistic wireless optical communication through the underwater-to-air system, it is necessary to analyze the impacts of air-sea interface and bubbles in the upper ocean layer.

The sea surfaces were modelled under different wind conditions, specifically at wind speeds of 3, 5 and 10 m s^{-1}. To generate these varied sea surfaces, The ECKV model was employed which accurately replicates the complex dynamics of ocean waves influenced by the varying wind speeds. The

spatial grid resolution for the sea surfaces generated in our simulations is an important consideration in the present study. When making the simplified assumption that the sea surface is perfectly flat, there are no spatial or temporal variations in its characteristics. Consequently, the power received by this flat surface remains constant regardless of the changes in time, wind speed or spatial location. Numerous studies have employed the Cox and Munk sea surface model to analyse the received power in wave surface conditions. However, it is important to note that this model does not provide a comprehensive explanation of the spatial and temporal dynamics of sea surfaces and wave shapes. When the model reveals variations in the received power with varying wind speeds, it is worth emphasising that for a single wind speed scenario, the received power remains constant. This suggests that the Cox and Munk model captures wind-dependent fluctuations in the received power without accounting for the intricate variations in the sea surface characteristics and waveforms that occur under these conditions.

In reality, sea surfaces exhibit a diverse range of wave shapes at different locations, which can encompass crests, troughs, and various random patterns. These complex waveforms introduce dynamic variations in the sea surface over time, making it a dynamic and ever-changing environment. Consequently, the received power from such dynamic sea surfaces can fluctuate considerably due to their temporal and spatial changes.

To investigate the influence of wave shape on the received power, the maximum wavelength (L_x and L_y) was divided into 500 cross-sectional segments for each wind speed. After travelling 50 m through the water, the optical beam passed through the segmented wave cross sections. Observed was a range of fluctuations in the laser beam's intensity at the receiver and this intensity variation was directly related to the specific wave shapes encountered on the sea surface. Consequently, the power received by the detector varied significantly depending on the specific characteristics of the encountered waves, highlighting the substantial impact of wave shape on the received power.

A. NORMALISED RECEIVED POWER

In our analysis, we examined the wind speeds of 3, 5, and 10 m s^{-1} and calculated the received power at the detector plane for each scenario by considering every cross section of the sea surface. The receiver aperture size FOV were considered as 4'' and 180^0 respectively. Our calculations revealed that the presence of waves can significantly impact the received power, potentially resulting in a reduction in the received power and consequently limiting the data transfer capability of the system.

In Fig. 11, we present a histogram depicting the fitting of normalised received power derived from the contributions of 500 distinct cross-sections under varying wind speeds. Our analysis revealed that the received power is not consistent for a specific wind speed, but it falls within a defined range that is influenced by the wind speed. When the wind speed reaches 10 m s^{-1}, the received power is observed to be lower compared to the cases with wind speeds 3 and 5 m s^{-1}. This observation suggests that with the increasing wind speed, the sea surface becomes rougher and leads to a more divergent orientation of the sea surface normal. Consequently, this variation of the sea surface roughness is directly reflected in the received power calculations, which highlight the sensitivity of the system's performance depending on the wind speed and sea surface conditions.

In addition, we investigated the received power variations in the presence of bubbles in the uppermost layers of the

TABLE 2. The Parameters used for MC simulations.

Parameter	Value
Transmitted beam power (P_{Tx})	50 mW
Transmitted beam divergence angle (θ)	1.5 mrad
Transmitted beam width (ω)	1 mm
Transmission beam wavelength (λ)	515 nm
Optical filter bandwidth ($\Delta\lambda$)	15 nm
Optical filter transmissivity (T_f)	1
Gain of APD (M_{APD})	50
TIA resistance (R_{TIA})	50 Ω
Responsivity of APD (R_{APD})	0.8 AW^{-1}
Receiver aperture	4 inches
Receiver FOV	90^0 - 180^0

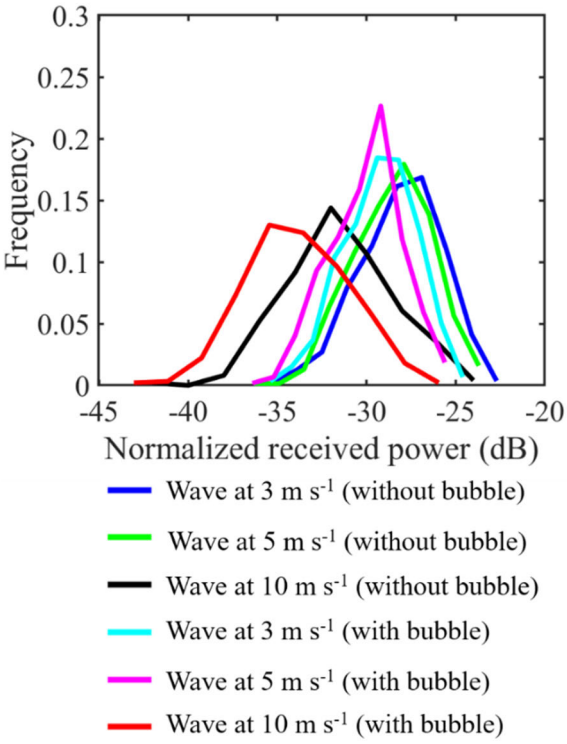

FIGURE 11. The histograms of the normalised received power (aperture: 5'', FOV: 180^0) for 500 sea surface cross-sections at various wind speeds.

sea surface. These bubbles penetrate into the subsurface layer depending on the wind speed. For the MC simulations, we determined the depth to which bubbles penetrated using an exponential decay model that considers the decreasing bubble concentrations with increasing water depth. Our analysis revealed that the wave-breaking-induced bubbles penetrate to water depths of 5, 7, and 10 m for wind speeds of 3, 5, and 10 m s^{-1} respectively.

Figure 11 shows the histograms of the normalised received power (with a 5'' aperture and a FOV 180^0) calculated based on the data collected from 500 different sea surface cross sections and all of which incorporated the bubbles. Our findings clearly demonstrate that the oceanic bubbles have a substantial impact on the normalised received power. When compared to the scenarios without bubbles, the received power significantly decreases under these conditions. Further observations revealed that the oceanic bubbles generated at various wind speeds introduce significant variations in the received power due to changes in the number density of bubbles according to wind speed fluctuations. The bubble number density fluctuation is of utmost importance for UOWC studies, as it directly influences both the scattering and attenuation coefficients. Specifically, at higher wind speeds, these coefficients are increased leading to the increased photon loss owing to a greater number of scattering events. A contributing factor to this phenomenon is that a photon scatters off a bubble at the higher angles when compared to other particulates in the water column. This scattering behaviour causes the optical beam to spread more quickly and widely, ultimately leading to a reduction in the received power intensity at the center of the beam.

B. UNDERWATER-TO-AIR OWC SYSTEM'S BER PERFORMANCE

This section presents a detailed analysis of numerical results to precisely quantify the influence of solar noise on the performance of a typical underwater-to-air OWC link operating in clear oceanic water conditions. We conducted a comprehensive assessment of the system's performance – specifically focusing on BER under various solar noise scenarios. These scenarios were dependent on the factors such as wind speeds, time of day, and bubbles in the upper ocean layer. It is important to note that our analysis assumes the ideal conditions, including perfect beam alignment and precise time synchronisation between the transmitter and the receiver. Data transmission is executed using NRZ-OOK modulation with a transmission speed of 500 Mbps, which allows us to rigorously evaluate the system's performance in realistic operational settings. In the system that employs NRZ-OOK modulation, the APD's bandwidth efficiency is set at 1 bit per second per hertz (1 bit/s/Hz). For this analysis, we have considered an APD receiver and the receiver parameters as provided in Table 2. In our study, we focused on a wavelength of 515 nm. To determine solar power for our analysis, we calculated it based on the solar spectrum specifically at this wavelength under investigation.

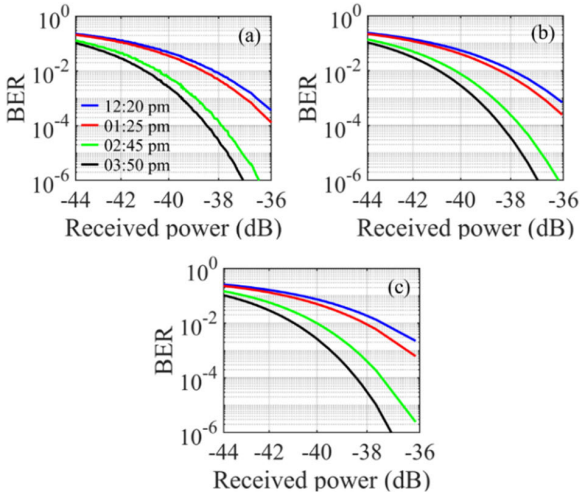

FIGURE 12. BER as a function of the received signal power with an APD receiver and the variations at different times of day and wind speeds (a) 3 m s^{-1}, (b) 5 m s^{-1}, and (c) 10 m s^{-1}.

1) THE IMPACT OF SOLAR NOISE ACROSS DIFFERENT TIMES OF THE DAY

As previously discussed, solar radiation exhibits varying intensities throughout the day. This fluctuation in solar intensity plays a crucial role in influencing the system BER performance in distinct ways at different times of the day. For this analysis, we assumed no bubbles present on the sea surface and performed the BER calculations with the different received signal power for particular wind speed conditions, which determine the shape of the surface waves and hence the solar power variations. Figure 12 presents the BER performance of an underwater-to-air OWC system. It demonstrates how the BER changes in response to the received signal power at different wind speeds and various times of the day. The simulations were executed using a receiver FOV value of 180^0. Our findings indicate that when the Sun passes through the zenith at noon, the BER exhibits poor performance across all wind speed conditions. This deterioration in BER performance is attributed to the increased collection of solar power around midday. As the sea surface wave shapes cause variations in the received signal power, it is imperative to identify the minimum power threshold as necessary to achieve the improved BER performance, aligned with the constraints of the Forward Error Correction (FEC) limit. According to our analysis, we have established specific minimum power requirements to achieve error-free data transmission at various times of the day. These requirements vary depending on the wind speed conditions, ensuring reliable communication in different scenarios.

2) THE IMPACT OF SOLAR NOISE IN THE PRESENCE OF SUN GLINT

The sun glint varies depending on its intensity at different wavelengths, Sun angle and sea surface conditions. In addition to the inherent solar noise from different sources, the sun glint radiation also interacts / interferes with the

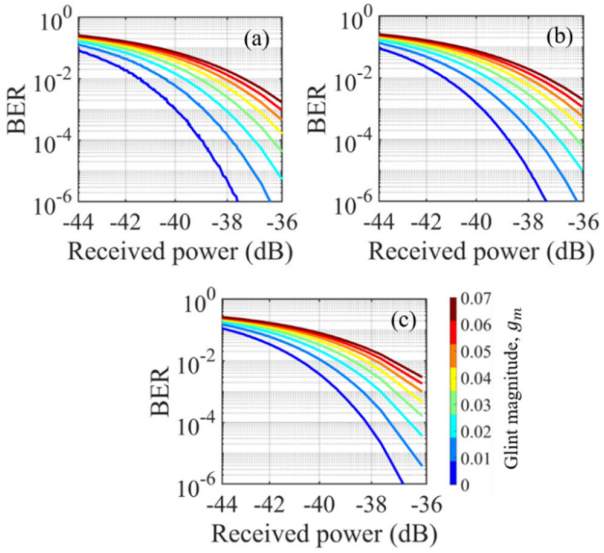

FIGURE 13. BER as a function of the received signal power around midday (noon time) with the varying glint intensities and wind speed conditions (a) 3 m s^{-1}, (b) 5 m s^{-1}, and (c) 10 m s^{-1}.

transmitted optical signal. This phenomenon of sun glint is particularly prominent when the Sun is around midday. In our study, we conducted a detailed analysis of the sun glint effect on the optical signal and system BER performance. For this analysis, the FOV was set at 90^0. Figure 13 shows the BER performance of the OWC system under various sun glint intensities when combined with the other sources of solar noise at wind speeds of 3, 5, and 10 m s^{-1}. The solid blue line on each graph represents the system's BER performance in the absence of sun glint and other solid lines of varying colors depict the BER performance at different sun glint intensities. Our results highlight the substantial impact of sun glint on the system's BER performance. It is noteworthy that if experiments or simulations are conducted on the conditions of maximum possible sun glint, it will become challenging to achieve error-free transmission at the lower received signal power and all wind speeds.

It should be noted that sun glint occurs throughout the day but exhibits higher intensities around midday (at high noon). Consequently, there are fluctuations in the system's BER performance due to the prevailing sun glint conditions. To avoid sun glint during the in-situ experiments in marine environments, one may consider scheduling these measurements during early morning or late afternoon hours when the sun is at a lower angle. Also to adjust the instrument angles and use polarising filters or anti-glare shields to minimise glare from the water's surface.

3) THE IMPACT OF SOLAR NOISE IN THE PRESENCE OF WAVE-INDUCED BUBBLES ON THE SEA SURFACE

Wave breaking is a common occurrence in the marine environments due to the prevailing winds. This oceanographic process generates bubbles in the upper ocean layer and hence it becomes virtually unavoidable to simulate the system's BER performance without accounting the oceanic bubbles.

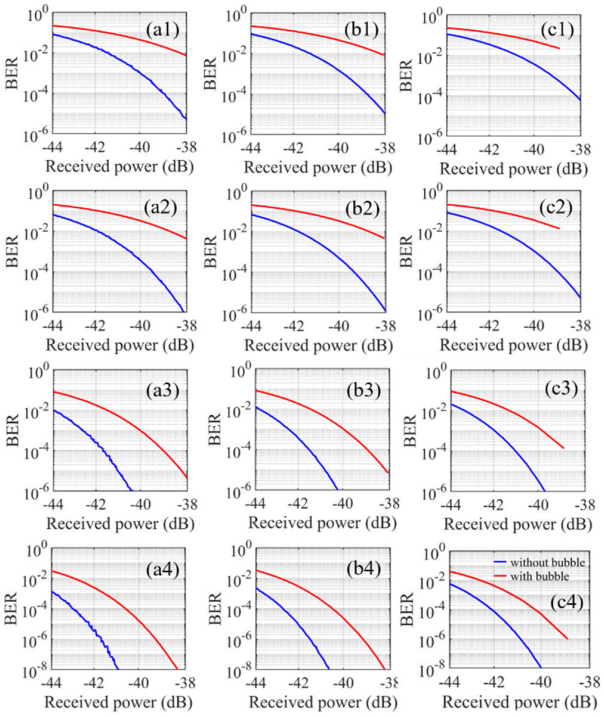

FIGURE 14. BER as a function of the received signal power at different times of the day and wind speeds with and without bubbles. Subplots (a1) through (a4) correspond to a wind speed of 3 m s^{-1}at 12:20 pm, 01:25 pm, 02:45 pm, and 03:50 pm, respectively. Subplots (b1) through (b4) correspond to a wind speed of 5 m s^{-1}, while subplots (c1) through (c4) represent a wind speed of 10 m s^{-1}.

In this study, we made a significant observation from our simulations. The presence of bubbles generated by wave breaking conditions results in distinct variations in the solar power collected at the receiver, in contrast to the scenarios in the absence of bubbles. In our measurements conducted at various times of the day, the wind speed was consistently observed around 5 m s^{-1} when making the measurements of upwelling solar radiance ($L_u\left(0^-\right)$). There were no $L_u\left(0^-\right)$ data collected for instances when bubbles were generated at wind speeds of 3 and 10 m s^{-1}. For these two wind speed conditions, we made the assumption that the solar radiation at the detector was similar to that at a wind speed of 5 m s^{-1}. Nevertheless, the transmittance parameter was taken into account that corresponds to the sea surfaces generated by wind speeds of 3 and 10 m s^{-1}. As a result, the solar noise reaching the detector differed from the condition at 5 m s^{-1} due to the variability of the transmittance parameter associated with the wind-generated sea surfaces. Figure 14 shows the BER performance of the underwater-to-air OWC system for two scenarios: with bubbles and without bubbles at different wind speeds, while considering a receiver FOV of 90^0. According to these simulations, the presence of bubbles in the uppermost ocean layer leads to a reduction in the transmitted power at the detector, and these bubbles have the effect of enhancing the solar radiation reaching the receiver. Consequently, the BER performance deteriorates when bubbles are present at the sea surface as compared to the system's performance in the absence of bubbles.

IV. CONCLUSION

A robust model was presented in this study for evaluating the performance of underwater-to-air OWC system using Monte Carlo technique. Using the simulation and experimental results, we comprehensively assessed the impact of solar noise on the system BER performance by taking into account the various marine environmental factors such as bubbles, wavy surface conditions, and solar noise under different atmospheric and marine conditions. To ensure an accurate simulation of the system's performance, we incorporated the in-situ optical measurements, including IOPs and solar radiance data obtained from Bay of Bengal waters. Additionally, the measurement data were collected from the Southern Ocean to derive and account for the bubble properties using the theoretical HN model. The modelling of wavy surface was achieved through the utilisation of the ECKV model, which incorporates both spatial and temporal dependencies in the generation of sea surfaces. This approach was crucial for our understanding of the optical signal behaviour when propagating through the air-sea interface. This study highlighted the significant influence of both sea wave shapes and bubbles on the received signal power of a laser beam at different wind speed conditions. The findings indicate that the received signal power varied depending on the wind speed and surface wave structure at the air-sea boundary. Additionally, the oceanic bubbles were found to decrease the received signal power as the wind speed increased. Finally, we analysed the system's BER performance under different times of the day, varying sun glint intensities, and different receiver setups. Our findings indicate that the BER performance is significantly deteriorated around midday (when the sun at noon) and improved at other times of the day. Additionally, we observed that the sun glint has a significant impact on the system's BER performance. The higher intensities of sun glint result in reduced BER performance, leading to an increased occurrence of data transmission errors. Additionally, our analysis revealed that the presence of bubbles in the upper ocean layer enhances the reception of solar signal power at the receiver. Consequently, this increase in solar power due to the oceanic bubbles leads to a reduction in the system's BER performance as compared to scenarios in the absence of bubbles. These findings offer essential guidance for system designers as they create and refine underwater-to-air OWC systems by taking into account the various marine and atmospheric conditions encountered in real-world applications.

REFERENCES

[1] A. Morel, B. Gentili, H. Claustre, M. Babin, A. Bricaud, J. Ras, and F. Tièche, "Optical properties of the 'clearest' natural waters," *Limnol. Oceanogr.*, vol. 52, no. 1, pp. 217–229, Jan. 2007, doi: 10.4319/lo.2007.52.1.0217.

[2] K. Nakamura, I. Mizukoshi, and M. Hanawa, "Optical wireless transmission of 405 nm, 145 Gbit/s optical IM/DD-OFDM signals through a 48 m underwater channel," *Opt. Exp.*, vol. 23, no. 2, p. 1558, 2015, doi: 10.1364/oe.23.001558.

[3] D. B. Kilfoyle and A. B. Baggeroer, "The state of the art in underwater acoustic telemetry," *IEEE J. Ocean. Eng.*, vol. 25, no. 1, pp. 4–27, Jan. 2000, doi: 10.1109/48.820733.

[4] Y. R. Zheng, "Channel estimation and phase-correction for robust underwater acoustic communications," in *Proc. IEEE Mil. Commun. Conf. (MILCOM)*, Oct. 2007, pp. 1–6, doi: 10.1109/MILCOM.2007.4454811.

[5] A. I. Al-Shamma'a, A. Shaw, and S. Saman, "Propagation of electromagnetic waves at MHz frequencies through seawater," *IEEE Trans. Antennas Propag.*, vol. 52, no. 11, pp. 2843–2849, Nov. 2004, doi: 10.1109/TAP.2004.834449.

[6] X. Che, I. Wells, G. Dickers, P. Kear, and X. Gong, "Re-evaluation of RF electromagnetic communication in underwater sensor networks," *IEEE Commun. Mag.*, vol. 48, no. 12, pp. 143–151, Dec. 2010, doi: 10.1109/MCOM.2010.5673085.

[7] H. Kaushal and G. Kaddoum, "Underwater optical wireless communication," *IEEE Access*, vol. 4, pp. 1518–1547, 2016, doi: 10.1109/ACCESS.2016.2552538.

[8] A. S. Fletcher, S. A. Hamilton, and J. D. Moores, "Undersea laser communication with narrow beams," *IEEE Commun. Mag.*, vol. 53, no. 11, pp. 49–55, Nov. 2015, doi: 10.1109/MCOM.2015.7321971.

[9] F. Hanson and S. Radic, "High bandwidth underwater optical communication," *Appl. Opt.*, vol. 47, no. 2, p. 277, 2008, doi: 10.1364/ao.47.000277.

[10] P. Rozmej, A. Karczewska, and E. Infeld, "Superposition solutions to the extended KdV equation for water surface waves," *Nonlinear Dyn.*, vol. 91, no. 2, pp. 1085–1093, Jan. 2018, doi: 10.1007/s11071-017-3931-1.

[11] C. Cox and W. Munk, "Measurement of the roughness of the sea surface from photographs of the Sun's glitter," *J. Opt. Soc. Amer.*, vol. 44, no. 11, p. 838, 1954, doi: 10.1364/josa.44.000838.

[12] T. Elfouhaily, B. Chapron, K. Katsaros, and D. Vandemark, "A unified directional spectrum for long and short wind-driven waves," *J. Geophys. Res., Oceans*, vol. 102, no. C7, pp. 15781–15796, Jul. 1997, doi: 10.1029/97jc00467.

[13] Y. Du, X. Yang, K.-S. Chen, W. Ma, and Z. Li, "An improved spectrum model for sea surface radar backscattering at L-band," *Remote Sens.*, vol. 9, no. 8, p. 776, Jul. 2017, doi: 10.3390/rs9080776.

[14] C. D. Mobley, "Polarized reflectance and transmittance properties of windblown sea surfaces," *Appl. Opt.*, vol. 54, no. 15, p. 4828, 2015, doi: 10.1364/ao.54.004828.

[15] A. Tanaka, H. Sasaki, and J. Ishizaka, "Alternative measuring method for water-leaving radiance using a radiance sensor with a domed cover," *Opt. Exp.*, vol. 14, no. 8, p. 3099, 2006, doi: 10.1364/oe.14.003099.

[16] K. G. Ruddick, K. G. Ruddick, K. Voss, E. Boss, A. Castagna, R. Frouin, A. Gilerson, M. Hieronymi, B. C. Johnson, J. Kuusk, Z. Lee, M. Ondrusek, V. Vabson, and R. Vendt, "A review of protocols for fiducial reference measurements of water-leaving radiance for validation of satellite remote-sensing data over water," *Remote Sens.*, vol. 11, no. 19, p. 2198, Sep. 2019, doi: 10.3390/rs11192198.

[17] D. D'Alimonte, T. Kajiyama, G. Zibordi, and B. Bulgarelli, "Sea-surface reflectance factor: Replicability of computed values," *Opt. Exp.*, vol. 29, no. 16, p. 25217, 2021, doi: 10.1364/oe.424768.

[18] R. Sahoo, S. K. Sahu, and P. Shanmugam, "Estimation of the channel characteristics of a vertically downward optical wireless communication link in realistic oceanic waters," *Opt. Laser Technol.*, vol. 116, pp. 144–154, Aug. 2019, doi: 10.1016/j.optlastec.2019.03.023.

[19] R. Sahoo and P. Shanmugam, "Effect of the complex air–sea interface on a hybrid atmosphere-underwater optical wireless communications system," *Opt. Commun.*, vol. 510, May 2022, Art. no. 127941, doi: 10.1016/j.optcom.2022.127941.

[20] Y. Dong, S. Tang, and X. Zhang, "Effect of random sea surface on downlink underwater wireless optical communications," *IEEE Commun. Lett.*, vol. 17, no. 11, pp. 2164–2167, Nov. 2013, doi: 10.1109/LCOMM.2013.091113.131363.

[21] J. Qin, M. Fu, and B. Zheng, "Analysis of wavy surface effects on the characteristics of wireless optical communication downlinks," *Opt. Commun.*, vol. 507, Mar. 2022, Art. no. 127623, doi: 10.1016/j.optcom.2021.127623.

[22] M. S. Islam and M. F. Younis, "Analyzing visible light communication through air–water interface," *IEEE Access*, vol. 7, pp. 123830–123845, 2019, doi: 10.1109/ACCESS.2019.2938522.

[23] T. Lin, N. Huang, C. Gong, J. Luo, and Z. Xu, "Preliminary characterization of coverage for water-to-air visible light communication through wavy water surface," *IEEE Photon. J.*, vol. 13, no. 1, pp. 1–13, Feb. 2021, doi: 10.1109/JPHOT.2021.3054911.

[24] D. Chen, P. Zhao, L. Tang, and M. Wang, "Modeling and oblique transmission characteristics of an underwater wireless optical communication channel based on ocean depth layering," *J. Opt. Soc. Amer. A, Opt. Image Sci.*, vol. 4, no. 3, pp. 424–434, 2024, doi: 10.1364/JOSAA.512023.

[25] C. S. S. Shetty, R. P. Naik, U. S. Acharya, and W.-Y. Chung, "Performance analysis of underwater vertical wireless optical communication system in the presence of weak turbulence, pointing errors and attenuation losses," *Opt. Quantum Electron.*, vol. 55, no. 1, pp. 1–22, Jan. 2023, doi: 10.1007/s11082-022-04283-6.

[26] M. Elamassie and M. Uysal, "Vertical underwater visible light communication links: Channel modeling and performance analysis," *IEEE Trans. Wireless Commun.*, vol. 19, no. 10, pp. 6948–6959, Oct. 2020, doi: 10.1109/TWC.2020.3007343.

[27] Y. Lou, J. Cheng, D. Nie, and G. Qiao, "Performance of vertical underwater wireless optical communications with cascaded layered modeling," *IEEE Trans. Veh. Technol.*, vol. 71, no. 5, pp. 5651–5655, May 2022, doi: 10.1109/TVT.2022.3156388.

[28] B. Rao Angara, P. Shanmugam, and H. Ramachandran, "Influence of sea surface waves and bubbles on the performance of underwater-to-air optical wireless communication system," *Opt. Laser Technol.*, vol. 174, Jul. 2024, Art. no. 110652, doi: 10.1016/j.optlastec.2024.110652.

[29] E. Lamarre and W. K. Melville, "Air entrainment and dissipation in breaking waves," *Nature*, vol. 351, no. 6326, pp. 469–472, Jun. 1991, doi: 10.1038/351469a0.

[30] S. A. Thorpe and P. N. Humphries, "Bubbles and breaking waves," *Nature*, vol. 283, no. 5746, pp. 463–465, Jan. 1980, doi: 10.1038/283463a0.

[31] L. Ma, F. Wang, C. Wang, C. Wang, and J. Tan, "Monte Carlo simulation of spectral reflectance and BRDF of the bubble layer in the upper ocean," *Opt. Exp.*, vol. 23, no. 19, p. 24274, 2015, doi: 10.1364/oe.23.024274.

[32] B. R. Angara, P. Shanmugam, and H. Ramachandran, "Underwater wireless optical communication system channel modelling with oceanic bubbles and water constituents under different wind conditions," *IEEE Photon. J.*, vol. 15, no. 2, pp. 1–11, Apr. 2023, doi: 10.1109/JPHOT.2023.3258500.

[33] W. H. Richey, S. Luminance, and J. E. Tyler, "Light in the sea," *J. Opt. Soc. Amer.*, vol. 53, no. 2, pp. 214–233, 1961.

[34] S. K. Mahapatra and S. K. Varshney, "Impact of orientation-based solar light noise on the performance of underwater optical wireless communication system and noise cancellation," *Results Opt.*, vol. 7, May 2022, Art. no. 100214, doi: 10.1016/j.rio.2022.100214.

[35] T. Hamza, M.-A. Khalighi, S. Bourennane, P. Léon, and J. Opderbecke, "Investigation of solar noise impact on the performance of underwater wireless optical communication links," *Opt. Exp.*, vol. 24, no. 22, p. 25832, 2016, doi: 10.1364/oe.24.025832.

[36] F. Xing and H. Yin, "Performance analysis for underwater cooperative optical wireless communications in the presence of solar radiation noise," in *Proc. IEEE Int. Conf. Signal Process., Commun. Comput. (ICSPCC)*, Sep. 2019, pp. 1–6, doi: 10.1109/ICSPCC46631.2019.8960742.

[37] X. Wang, M. Zhang, H. Zhou, and X. Ren, "Performance analysis and design considerations of the shallow underwater optical wireless communication system with solar noises utilizing a photon tracing-based simulation platform," *Electronics*, vol. 10, no. 5, p. 632, Mar. 2021, doi: 10.3390/electronics10050632.

[38] S. K. Mahapatra and S. K. Varshney, "Performance of the Reed–Solomon-coded underwater optical wireless communication system with orientation-based solar light noise," *J. Opt. Soc. Amer. A, Opt. Image Sci.*, vol. 39, no. 7, p. 1236, 2022, doi: 10.1364/josaa.453257.

[39] R. S. Keiffer, J. C. Novarini, and G. V. Norton, "The impact of the background bubble layer on reverberation-derived scattering strengths in the low to moderate frequency range," *J. Acoust. Soc. Amer.*, vol. 97, no. 1, pp. 227–234, Jan. 1995, doi: 10.1121/1.412990.

[40] K. Randolph, H. M. Dierssen, M. Twardowski, A. Cifuentes-Lorenzen, and C. J. Zappa, "Optical measurements of small deeply penetrating bubble populations generated by breaking waves in the Southern Ocean," *J. Geophys. Res., Oceans*, vol. 119, no. 2, pp. 757–776, Feb. 2014, doi: 10.1002/2013jc009227.

[41] X. Zhang, M. Lewis, M. Lee, B. Johnson, and G. Korotaev, "The volume scattering function of natural bubble populations," *Limnol. Oceanogr.*, vol. 47, no. 5, pp. 1273–1282, Sep. 2002, doi: 10.4319/lo.2002.47.5.1273.

[42] C. D. Mobley, "Estimation of the remote-sensing reflectance from above-surface measurements," *Appl. Opt.*, vol. 38, no. 36, p. 7442, 1999, doi: 10.1364/ao.38.007442.

[43] Z. Lee, Y.-H. Ahn, C. Mobley, and R. Arnone, "Removal of surface-reflected light for the measurement of remote-sensing reflectance from an above-surface platform," *Opt. Exp.*, vol. 18, no. 25, p. 26313, 2010, doi: 10.1364/oe.18.026313.

[44] P. J. Dev and P. Shanmugam, "A new theory and its application to remove the effect of surface-reflected light in above-surface radiance data from clear and turbid waters," *J. Quant. Spectrosc. Radiat. Transf.*, vol. 142, pp. 75–92, Jul. 2014, doi: 10.1016/j.jqsrt.2014.03.021.

[45] S. Liu, N. Jia, and C. Guan, "A proposed frequency spectrum for fully developed wind waves by revisiting P-M spectrum," *J. Ocean Univ. China*, vol. 10, no. 4, pp. 331–335, Dec. 2011, doi: 10.1007/s11802-011-1804-7.

[46] G. Giuliano, L. Laycock, D. Rowe, and A. E. Kelly, "Solar rejection in laser based underwater communication systems," *Opt. Exp.*, vol. 25, no. 26, p. 33066, 2017, doi: 10.1364/oe.25.033066.

BHOGESWARA RAO ANGARA received the B.Tech. degree in electronics and communication engineering (ECE) from Andhra University, Andhra Pradesh, India, in 2011, and the M.Tech. degree in control and instrumentation from Delhi Technological University (DTU), Delhi, India, in 2015. He is currently a Ph.D. Scholar with the Department of Ocean Engineering and Electrical Engineering, IIT Madras, Chennai, India. His research interest includes underwater wireless optical communications (UWOC).

PALANISAMY SHANMUGAM received the Ph.D. degree in optical remote sensing from Anna University, Chennai, India, in 2002.

He is currently a Professor with the Department of Ocean Engineering, IIT Madras, Chennai, India, where he is involved in the experimental and theoretical studies of the optical properties of natural water, air–sea interface, and subsea optical processes. He has been a principal investigator of several projects funded by the Government of India. His current research interests include developing models for ocean optical studies and retrieval algorithms for multispectral and hyperspectral remote sensing sensors, with an emphasis on applications to sediment dynamics, algal blooms, climate change, and marine environmental and coastal processes.

HARISHANKAR RAMACHANDRAN received the B.Tech. degree from IIT Bombay, in 1982, and the Ph.D. degree from the University of California at Berkeley, both in electrical engineering.

He was a Research Scientist with the Physics Department, University of California at Los Angeles, for five years before returning to India. He was a Scientist with the Institute for Plasma Research, Gandhinagar, from 1993 to 2001. In November 2001, he joined IIT Madras, where he is currently a Professor with the Department of Electrical Engineering. His research interests include optical link design and planning, nonlinear optics, computational optics, edge plasma physics, and computational plasma physics.

CHAVAPATI GOUSE SANDHANI received the B.Tech. degree in civil engineering from API-IIT Nuzvid, RGUKT University, Nuzvid, Andhra Pradesh, India, in 2015, and the M.Tech. degree in environmental engineering and management from IST, JNTUK University, Kakinada, Andhra Pradesh, in 2018.

He has been a Ph.D. Scholar with the Department of Ocean Engineering, IIT Madras, Chennai, India. His research work involves effect of bubble clouds on the remote sensing reflectance and deriving the water color products with and without bubble clouds.